Sea Ice - Atmosphere Interaction
Application of Multispectral Satellite Data in Polar Surface Energy Flux Estimates

K. Steffen, A. Schweiger, J. Maslanik, J. Key, R. Weaver, R. Barry
Cooperative Institute for Research in Environmental Sciences
Campus Box 449, University of Colorado, Boulder

NAGW - 2158

Progress Report
to
National Aeronautics and Space Administration
(Goddard Space Flight Center)

November 1990

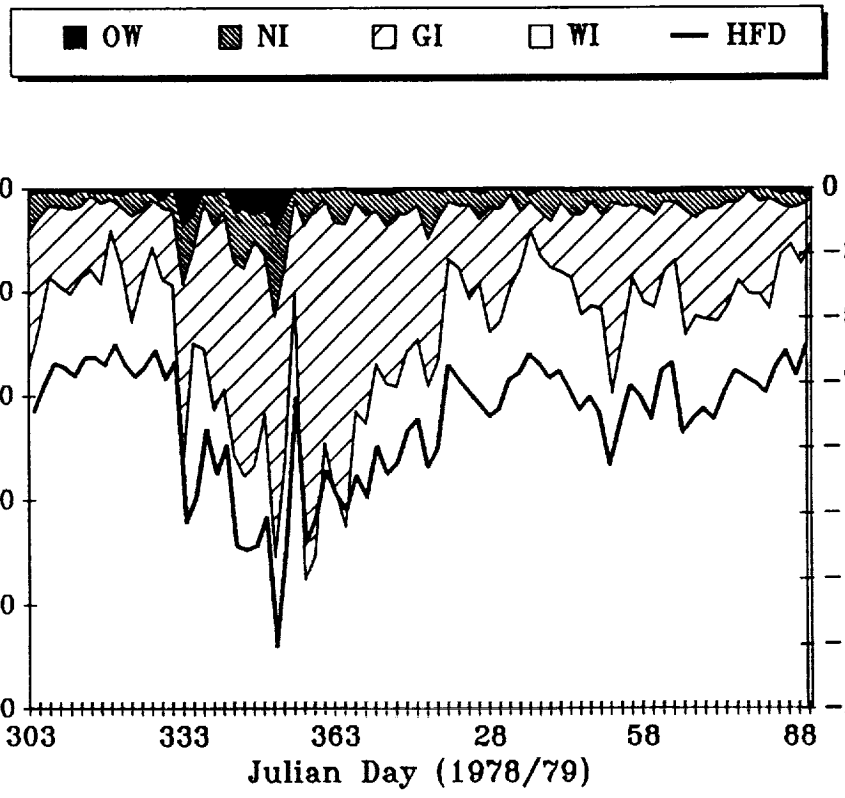

Table of Content

1. Objectives

The research involves the application of multi-spectral satellite data to estimate polar surface energy fluxes. The work is interdisciplinary, drawing upon our collective background and experience in the fields of climatology, oceanography, and remote sensing.

Our goal is to investigate to what accuracy and over which geographic areas large scale energy budgets can be estimated based upon a combination of available remote sensing and climatological data sets. Our general approach will be to:

(1) formulate parameterization schemes for the appropriate sea ice energy budget terms based upon the remotely sensed and/or in-situ data sets;

(2) conduct sensitivity analyses using as input both natural variability [observed data in regional case studies] and theoretical variability based upon energy flux model concepts;

(3) assess the applicability of these parameterization schemes to both regional and basin wide energy balance estimates using remote sensing data sets. In order to accomplish the above three objectives, we must also

4) assemble multi-spectral, multi-sensor data sets for at least two regions of the Arctic Basin and possibly one region of the Antarctic. We will also describe the type of data needed for a basin-wide assessment. The temporal coverage of these data sets will be determined by data availability, and need as defined by parameterization scheme.

The concept of surface energy flux parametrization over sea ice using satellite and meteorological data is shown in the following flow diagram. The main objective during the first phase of this project was to conduct various sensitivity tests with satellite data and with applied algorithm in view of energy flux parametrization.

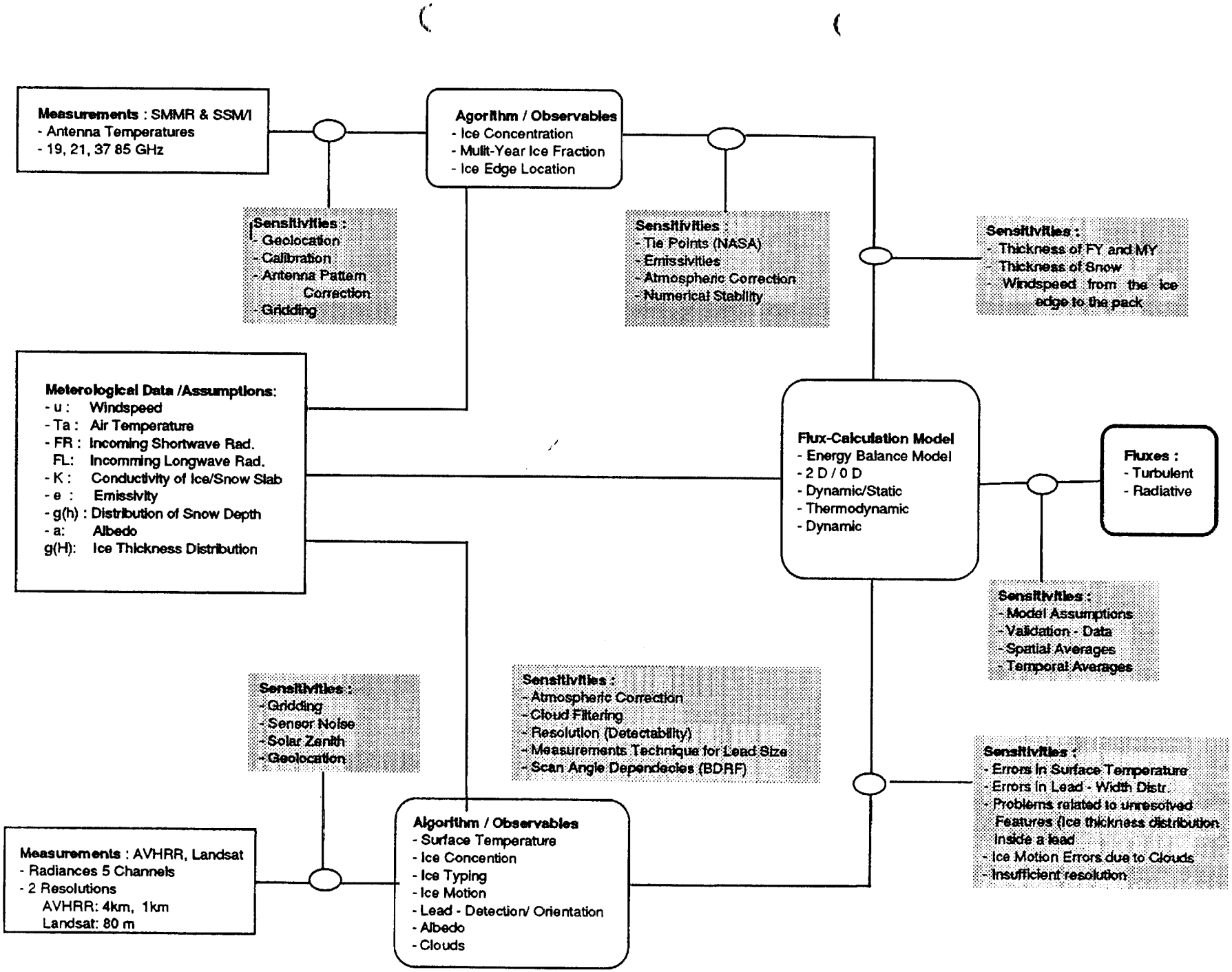
Measurements : SMMR & SSM/I
- Antenna Temperatures
- 19, 21, 37 85 GHz
Agorithm / Observables
- Ice Concentration
- Mulit-Year Ice Fraction
- Ice Edge Location
Sensitivities :
- Geolocation
- Calibration
- Antenna Pattern Correction
- Gridding
Sensitivities :
- Tie Points (NASA)
- Emissivities
- Atmospheric Correction
- Numerical Stability
Sensitivities :
- Thickness of FY and MY
- Thickness of Snow
- Windspeed from the ice edge to the pack
Meterological Data /Assumptions:
- u : Windspeed
- Ta : Air Temperature
- FR : Incoming Shortwave Rad.
FL: Incomming Longwave Rad.
- K : Conductivity of Ice/Snow Slab
- e : Emissivity
- g(h) : Distribution of Snow Depth
- a: Albedo
g(H): Ice Thickness Distribution
Flux-Calculation Model
- Energy Balance Model
- 2 D / 0 D
- Dynamic/Static
- Thermodynamic
- Dynamic
Fluxes :
- Turbulent
- Radiative
Sensitivities :
- Model Assumptions
- Validation - Data
- Spatial Averages
- Temporal Averages
Sensitivities :
- Gridding
- Sensor Noise
- Solar Zenith
- Geolocation
Sensitivities :
- Atmospheric Correction
- Cloud Filtering
- Resolution (Detectability)
- Measurements Technique for Lead Size
- Scan Angle Dependecies (BDRF)
Sensitivities :
- Errors in Surface Temperature
- Errors in Lead - Width Distr.
- Problems related to unresolved Features (Ice thickness distribution inside a lead
- Ice Motion Errors due to Clouds
- Insufficient resolution
Measurements : AVHRR, Landsat
- Radiances 5 Channels
- 2 Resolutions
AVHRR: 4km, 1km
Landsat: 80 m
Algorithm / Observables
- Surface Temperature
- Ice Concention
- Ice Typing
- Ice Motion
- Lead - Detection/ Orientation
- Albedo
- Clouds

2. Heat Flux Calculations from SSM/I and Landsat Data in the Bering Sea

2.1 Objective

This study is part of an overall attempt to quantify the magnitude of error in the calculation of turbulent fluxes from low resolution SSM/I data. Since no accurate data on directly measured fluxes are available for many areas of the Arctic ocean, estimates of error introduced by the low resolution SSM/I passive microwave data are obtained through comparison with higher resolution Landsat data that were simultaneously recorded during the SSM/I validation experiment in March 1988 (Steffen and Schweiger, submitted). This case study is designed to provide insights into the relative importance of flux-relevant data that can be obtained from high versus lower resolution sensors. In particular, the relative magnitude of error introduced by the coarse resolution in ice type and ice thickness that is possible from current SSM/I ice concentration algorithms, versus the sensitivity of heat flux calculations to the variation in fetch (ie. lead size).

2.2 Data

2.2.1 Landsat Data

Landsat data obtained for the SSM/I-validation experiment during March 1988 are used to obtain information regarding the approximate distribution of ice thickness. Data are acquired in form of photographic transparencies which are subsequently digitized, corrected for sensor noise and sun-angle effects and registered to the SSM/I projection [Steffen and Schweiger, 1990]. Ice thickness distributions statistics for individual 25x25 km SSM/I grid boxes are obtained using the following procedure.

Ice type classification from Landsat MSS imagery is possible because the penetration and reflection of short wave radiation at the ice surface is related to ice thickness. The thinner the ice, the darker it appears in the imagery. This relationship between ice albedo and thickness was quantified by Weller (1972). Comparison of Landsat-derived estimates with ground reflectance measurements during the AIDJEX experiments indicate that ice thickness can be distinguished up to 0.6 m with possible accuracies of 0.05 m when climatologically derived growth rates are incorporated for calibration [Hall, 1980]. In the present study, since no in situ measurements where made, ice type categories were determined subjectively based on reflectivity (no calibration to albedo was possible due to the photographic recording and digitization process) and context (e.g. time of the year, location with respect to lead). By interactively selecting appropriate thresholds, images were generally classified into the five following ice type classes, each corresponding to a particular thickness range according to a commonly used classification scheme [Steffen , 1986] :

Open Water/Black Nilas [OW/BN]	0.0 - 0.05 m
Light Nilas [LN]	0.05 - 0.10 m
Grey Ice [GI]	0.10 - 0.15 m
Grey - White Ice [GW]	0.15 - 0.30 m
White Ice [WI]	> 0. 3 m

TABLE 1. Ice classes and corresponding thickness categories (Steffen, 1986)

For this study a total of 5 Landsat scenes were analyzed. After elimination of cloud contaminated areas, ice thickness statistics for a total of 87 grid cells (25x25 km) could be computed. Ice type statistics for the entire area (5 Landsat scenes) are shown in Table 2.

Open Water/Black Nilas	3.31 %
Light Nilas	4.47 %
Grey Ice	13.13 %
Grey-White Ice	51.18 %
White Ice	26.91 %

TABLE 2. Concentrations of 5 different Ice types derived from 5 Landsat images in the Bering Sea during March 1988

2.2.2 SSM/I Data

SSM/I brightness temperatures for the 19 and 37 GHz channels were obtained from the National Snow and Ice Data Center' s digital archive (NSIDC, CIRES/University of Colorado at Boulder) and gridded to the SSM/I projection using a polar grid. The NASA-Team algorithm [Gloersen and Calvalieri, 1986] using "global" tie points [Cavlieri pers. Com.] was applied to the gridded brightness temperature to calculate ice concentrations. Only total ice concentrations were used in this study due to the absence of multi-year ice in this marginal ice zone area. Through comparison with Landsat data an error in the ice concentrations derived from SSM/I could be determined according to Equation 2.1. Total amount or first-year ice and open water for the area corresponding to the 5 Landsat scenes is shown in Table 3. A comparison with Landsat data allowed an estimate of the error in the ice concentrations which amounted to 5.2 % underestimation in ice concentration due to the presence of thin ice (Steffen and Schweiger, submitted).

$$\overline{IC} = \frac{\sum_{I=1}^{N} |IC(i)_{SSM/I} - IC(i)_{Landsat}|}{N} \qquad (2.1)$$

where N number of gridcells

$\overline{IC}$ mean error in ice concentrations

NASA-Team Algorithm Ice Concentration:	First -Year Ice	91.5 %
	Open Water	8.5 %
Landsat Ice Concentration:	First - Year Ice	96.7%
	Open Water	3.3 %

TABLE 3. Ice concentrations derived from SSM/I using the NASA-Team algorithm with "global" tie-points, and ice derived from Landsat data. Landsat ice concentrations were calculated as the sum of all ice types except black nilas. Black nilas is counted as open water. The Landsat ice concentrations represent the ice concentrations that would be calculated from SSM/I data if no error was present.

2.2.3 Atmospheric Data and Radiation Data

For the calculation of the energy balance data on incoming long-wave and short-wave radiation, air temperature, wind speed and relative humidity are needed. For this case study, the tabulated values of Maykut [1978] were used, which were derived from climatological data compiled by Doronin [1963], and modelling results by Maykut [1978]. The values utilized in the present study are given in Table 4.

Shortwave Radiation	8.0 [Wm^{-2}]
Incoming Longwave Radiation	164.9 [Wm^{-2}]
Air Temperature	- 33.8 [C]
Relative Humidity	90 %
Wind Speed	5 [m sec^{-1}]
Surface Pressure	1013 [mbar]
Water Temperature	-1. 8 [C]

Table 4: Climatological input data for heat flux calculations [after Maykut, 1978]

2.3 Energy Balance Model

Turbulent exchange of energy between ice/ocean and the atmosphere given the above tabulated conditions is mainly a function of surface temperature. Since surface temperature is not being directly measured by the sensors involved in this study, and is highly dependent on ice thickness, a simple energy balance model was used to calculate surface temperatures. The derived surface temperature is bounded to balance the radiative, turbulent and conductive fluxes. Turbulent fluxes are computed using a bulk transfer formulation. The energy balance model used in this study is essentially the one devised by Maykut [1978], with modifications for adjustable heat transfer coefficient based on the formulation by Andreas and Murphy [1987], and is given in Equation 2.2.

$$(1 - \alpha) F_r - I_0 + F_L - F_E + F_s + F_e + F_c = 0 \qquad (2.2)$$

where
- α albedo
- F_r incoming shortwave radiation
- I_0 amount of shortwave radiation penetrating the ice
- F_L incoming longwave radiation
- F_E emitted longwave radiation
- F_S sensible heat flux
- F_e latent heat flux
- F_c heat conduction through the ice

F_r and F_L are specified as input parameters. The amount of penetrating shortwave radiation into the ice (I_0) is parameterized in dependence of ice thickness (H) according to Maykut [1982] as :

$$I_0(H) = 0.805[1 - \alpha(H)]F_r e^{-1.5(H-0.1)} \qquad \text{for } 0.1 < H < 1 \text{ m} \qquad (2.3)$$

Albedo in dependence of H is parameterized as :

$$\alpha(H) = 0.44H^{.28} + 0.08 \qquad (2.4)$$

The conductive heat flux through the ice is dependent on the gradient of temperature between the surface and the bottom of the ice pack which is assumed to be linear for ice thickness H < 0.8 m [Maykut ,1978). F_c can then be written :

$$F_c = \psi(T_f - T_0) \qquad (2.5)$$

where ψ thermal conductance of the ice slab [ψ = ki ks/(ksH + ki h)]

H ice thickness

h thickness of snow layer

k_s, k_i conductivity coefficients for snow and ice

T_f temperature of the water at freezing = 1.8 °[C]

T_0 surface temperature

Emitted longwave radiation is given by the Stefan Boltzman equation:

$$F_E = \varepsilon\varepsilon_0 T_0^4 \tag{2.6}$$

where ε_0 emission coefficient

ε Stefan Bolzman constant

Turbulent fluxes are calculated using a bulk transfer formulation :

$$F_s = \rho c_p C_s u (T_a - T_0) \tag{2.7}$$

$$F_e = \rho L C_e u(q_a - q_{0)} \tag{2.8}$$

where ρ average air density

c_p specific heat at constant pressure

L latent heat of vaporization

q_a, q_0 specific humidity at reference height and surface respectively

T_a, T_0 air temperature at reference height and surface respectively

u wind speed at reference height

C_s, C_e bulk heat transfer coefficients for sensible and latent heat flux

Substitution of the individual term in Equation 2.2 and assuming known values for air temperature, humidity, wind speed and radiative fluxes as well as fixed transfer coefficients for C_s, and C_e for latent and sensible flux, Equation 2.2 can be solved using a numerical root finding procedure. While Maykut assumed fixed heat transfer coefficients for sensible and latent heat of $C_s = C_e = 1.75\ 10^{-3}$ for ice thicker that 1 m and $C_s = C_e = 3.0\ 10^{-3}$ for thin ice, recent formulation by Andreas and Murphy (1987) allow the calculation transfer coefficients that are adjusted for the effects of fetch and stability modification over thin ice and open water.

Substituting Equations 2.6 ,2.7 and 2.8 into Equation 2.2 , and inserting C_s and C_e as functions of u, T_0, T_a, relative humidity r and fetch X as derived by Andreas and Murphy (1987), Equation 2.2 can be rewritten as :

$$(1- \alpha(H))F_r - I_0(H) + F_L-\varepsilon T_0^4 + \rho c_p u C_s(u,T_0,T_a,X,r) (T_a- T_0)$$
$$+ \rho L u C_e(u,T_0,T_a,X,r)(q_a- q_0) + F_c(T_0,H,h) = 0 \qquad (2.8)$$

where

$C_s(u,T_0,T_a,X,r,z) = C_e(u,T_0,T_a,X,r,z)$: fetch and stability adjusted heat transfer coefficients according to Andreas and Murphy (1987),

X	fetch
r	relative humidity at reference height z
z	reference height
q_a, q_0	vapor densities (parametrized)

Equation 2.8 is solved for T_0 using a biscection root finding method. The more rapidly converging Newton - Raphson method employed by Maykut in his 1978 formulation requires the specification of derivatives, which are cumbersome to compute for the formulation using variable heat transfer coefficients. Using the biscection method the model still converges very rapidly.

While Maykut's formulation (Equation 2.1) has been used to calculate the sensitivity of ocean-atmosphere exchange over varying ice thicknesses, the above formulation including fetch sensitive heat transfer coefficients allows the evaluation of the sensitivity of heat flux calculations to varying lead sizes. From this sensitivity calculation we also expect an estimate as to how important information on lead sizes is in relation to the importance of ice thickness.

2.4 Results

2.4.1 Estimates of Fluxes over Different Ice Thickness Categories

Using the energy balance model described above and the data on air temperature, wind speed, short- and longwave radiation values from Maykut (1978), as described above, turbulent fluxes were calculated for different ice thickness categories assuming fetches of 10, 100 and 500 meters. The results are summarized in Figure 2.1. In addition, turbulent flux calculations using a fixed transfer coefficient for thinner ice of $3\ 10^{-3}$ as assumed by Maykut, is plotted for comparison. From this graph it is obvious, that the importance of fetch decreases rapidly with increasing ice thickness and is most significant for ice thinner than 0.1 m. For the ice thickness categories 0 - 0.1 m and 0.2 to 0.4 m the difference in turbulent fluxes between an 10 and a 500 m fetch are similar in size to an increase in ice thickness to the next category. In comparison to turbulent fluxes calculated using a fixed transfer coefficient of $3\ 10^{-3}$ turbulent fluxes for all but 10 meter fetches are lower. This indicates that the value of $3\ 10^{-3}$ is too high for situations where fetches exceed 10 meters.

2.4.2 Large Scale Flux Estimates

To investigate the relative importance of fetch in comparison to ice thickness in a larger scale context, area weighted flux averages were calculated for the thickness distributions given in Tables 2.1 and 2.2 assuming different fetches of 10 and 100 m. The results of these calculations are summarized in Figures 2.2 and 2.3. Individual categories in Figures 2.2 and 2.3 depict turbulent fluxes calculated using the Landsat derived ice thickness distribution with the following thicknesses assigned to the five ice thickness classes: open water/black nilas 0.05 m (Fig. 2.2), 0.00 m (Fig. 2.3.); light nilas 0.10 m; grey ice 0.15 m; grey-white ice 0.3 m; and white ice 1.0 m. For the categories SSM/I (error) and SSM/i (no error), ice concentrations are translated to ice thickness distribution by assigning a 1 m thickness to the FYI area and a 0.05 m (Fig. 2.2) or 0.0 m (Fig. 2.3) thickness to the open water areas. For all categories, a snow cover of 0.1 m was assumed to be present on ice thicker than 1.0 m.

The results demonstrate that for the conditions in the marginal ice zone, fetch is only of secondary importance of large scale turbulent fluxes, while the importance of ice thickness dominates. The absence of detailed thickness information leads to an underestimation of turbulent fluxes by roughly 50 % by the SSM/I ice concentration algorithm. This underestimation in fluxes would increase further even the SSM/I algorithm were to report accurate ice concentrations. Thus it is obvious, that the error in SSM/I derived ice concentrations due to the presence of large areas of thinner ice does only little to reduce the error in large scale flux estimates. Though the direction of this underestimation of ice concentrations is to reduce the error in large scale flux estimates, it is not sufficient to correct for the considerable error introduced by the lack of detailed ice thickness information. A comparison of Figures 2.2 and 2.3 shows the significant change in large scale fluxes, when the thinnest ice category is considered open water. Under the assumption of a 10 m fetch, turbulent fluxes almost doubled in the SSM/I category when the thinnest ice category is set to open water. This result has particular significance, in light of the SSM/I validation experiment. Due to our inability to distinguish between open water and black nilas in the Landsat imagery that was utilized for the comparison with SSM/I data, open water and black nilas were lumped into one category. In this sense we defined ice concentration as the sum of all ice types per unit area, that were thicker than 0.05 m. Thus, in effect we cannot be sure of the ice thickness of the "open water fraction " (as paradox as this may sound) which may vary between 0.00 and 0.05 m.

2.4.3 Sensitivity of Heat Fluxes to Wind Speed

The sensitivity of net heat input to the atmosphere $F_n = - F_c$ to changes in wind speed (Figs. 2.4 and 2.5) show the variation of F_n to an 80 % increase and 80 % decrease in wind speed from a mean value of 5.2 m s^{-1} respectively. Variations were calculated over different ice thicknesses.

Sensitivity of a variation in wind speed decreases dramatically with ice thickness and is up to 7 times as large over 0.1 m thick ice compared to over 0.3 m thick ice. We have yet to investigate the significance of the wind speed sensitivity in relation to the importance of ice thickness and fetch in a larger area context.

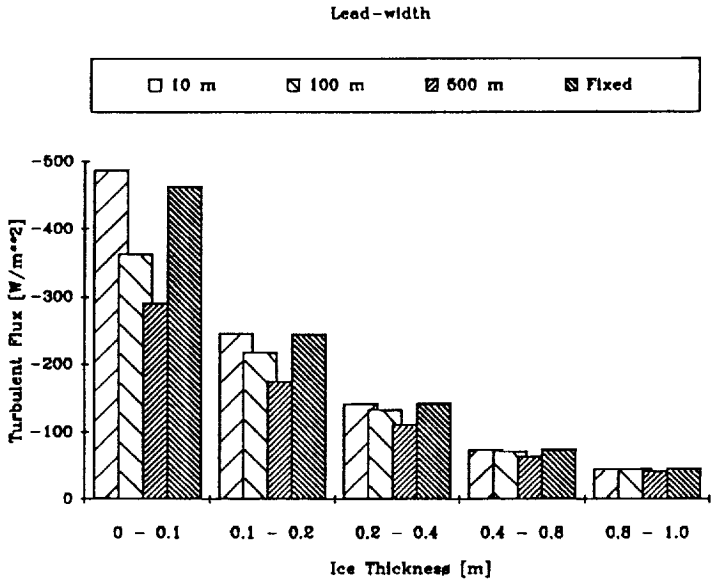

Fig. 2.1 Sensitivity of turbulent heat exchange over different ice thickness categories to lead width (fetch). For the forth class (Fixed), a fixed heat transfer coefficient of 3 10^{-3} was used.

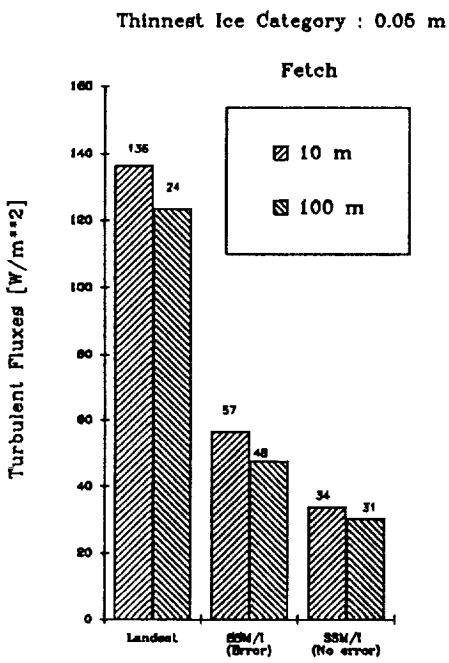

Fig 2.2

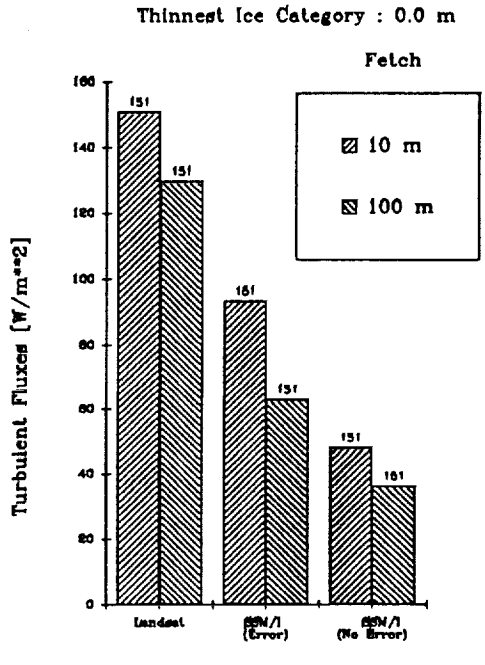

Fig. 2.3

Large scale turbulent fluxes for an area in the marginal ice zone during March in the Bering Sea computed from Landsat ice thickness distributions and SSM/I ice concentrations. Fig. 2.2: thinnest ice category is assumed to correspond to 0.05 m thickness,; Fig. 2.3: only thinnest category of ice is assumed to be open water.

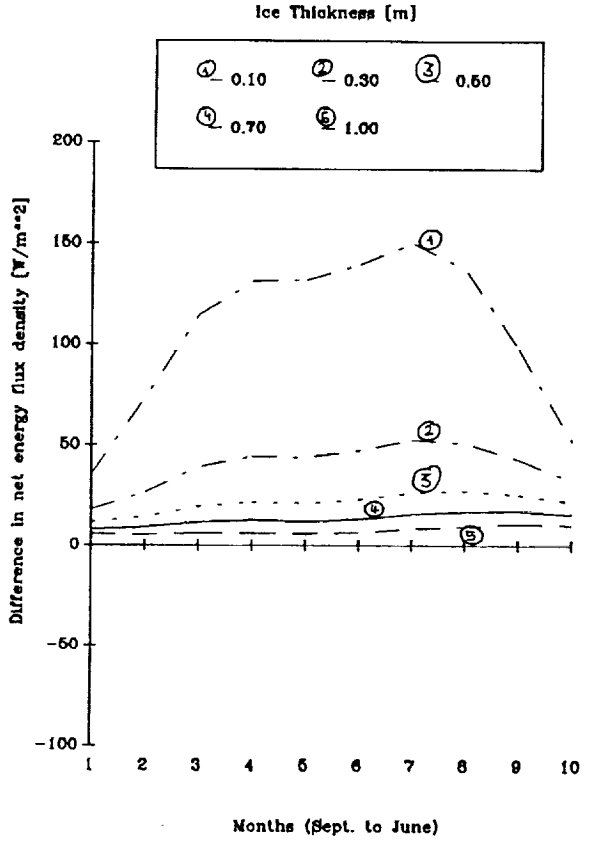

Fig. 2.4 Sensitivity of net heat input to the atmosphere (ocean -> atmosphere) to a 80 % decrease in windspeed from a mean of 5.2 m s-1. Note that a positive value corresponds to a decrease in net input to the atmosphere.

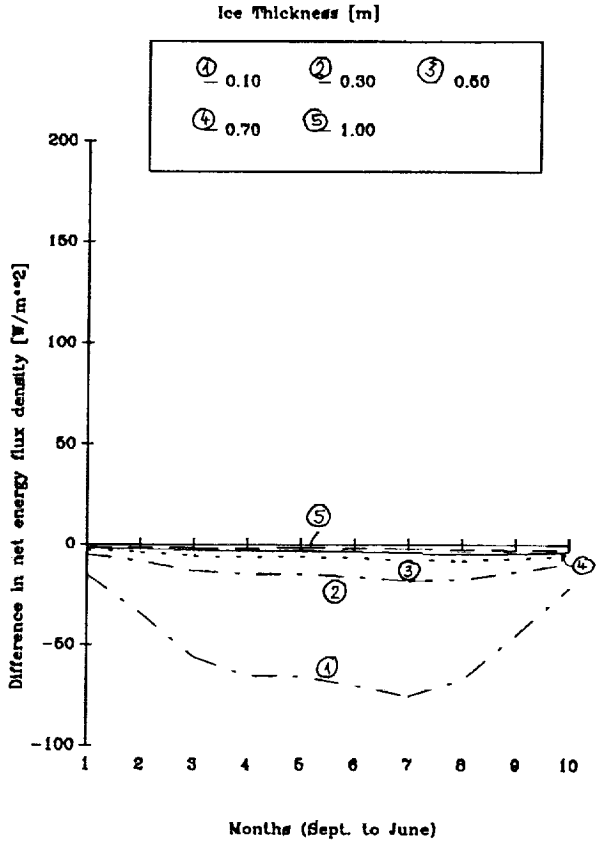

Fig. 2.5 Sensitivity of net heat input to the atmosphere (ocean -> atmosphere) to a 80 % increase in windspeed from a mean of 5.2 m/sec. Note that a positive value corresponds to an increase in net input to the atmosphere.

3. Energy Flux Estimation Using Passive Microwave Data

3.1. Introduction

With the launch of Nimbus 7 scanning multi-frequency microwave radiometer (SMMR) in 1976, for the first time the Arctic Ocean surface could be monitored at different frequencies and polarizations throughout the polar night [Cavalieri et al., 1984; Comiso, 1986; Gloerson and Cavalieri, 1986; Parkinson et al., 1987]. The ability of SMMR to acquire imagery of the earth's surface in most weather and under all lightning conditions makes SMMR particular useful for sea ice studies in polar regions. Based on a multi-frequency algorithm using 18 and 37 GHz at vertical and horizontal polarization, ice concentrations during winter and spring can be derived with a mean difference of 2.5 % (compared to the Landsat ice concentration) and a standard deviation of 6.4 % using the NASA-Team algorithm with global tie points [Steffen and Schweiger, submitted]. For the North Water area, a polynya in the northern Baffin Bay, the knowledge of ice type distribution is important for determining large-scale heat input at the ice-atmosphere boundary. Despite the extremely rapid decrease in energy exchange rates as ice forms in open water, young ice with a thickness of 0.3 m still has a net heat loss an order of magnitude larger than that of thick first-year ice [Maykut, 1978]. The snow cover on sea ice has an insulation effect on conduction. On the other hand, recent measurements by Crocker [1984] have shown that the snow cover overlying young ice contains large quantities of salt. This increases the thermal conductivity of the snow by up to 50 %. The thermal conductivity of snow on young ice is, however, still five times smaller than that of ice. In the North Water region, the snow cover on young ice, nilas and new ice will not exceed 20 mm in thickness [Steffen, 1986], and therefore, the insulation effect of the snow is negligible. For surface energy flux density estimates over polynyas, the percentage of open water and young ice types such as nilas (0 - 0.1 m) and grey to grey-white ice (0.1 - 0.3 m) are of prime interest.

In the following a method will be proposed to classify the above mentioned ice types based on passive microwave satellite measurements. The study area for which the ice type classification and the corresponding energy flux density estimation was carried out is delineated by longitude 70° and 80° W and parallels 72° N and 80° N. The ocean surface of the study area in northern Baffin Bay comprises approximately 100,000 km^2.

3.2 Method

3.2.1 Ice Typing

Microwave scattering of sea ice is due to the inhomogeneity of density and structure variations, whereas microwave absorption is mainly determined by the presence of liquid inclusions (brine volume). The relationship between the vertically polarized brightness temperatures and sea-ice properties such as brine volume or porosity are well known [Mätzler et al., 1984], whereas the horizontally polarized brightness temperature is sensitive to surface roughness. In a previous study it was found that the polarization ratio at 18 and 37 GHz increases with decreasing ice thickness [Steffen and Maslanik, 1988]. The polarization ratio is defined as:

$$PR_{fg} = (T_B(V,fq) - T_B(H,fq))) / (T_B(V,fq) + (T_B(H,fq)) \quad (3.1)$$

where PR_{fq} is the polarization ratio at frequency fq, $T_B(V,fq)$ and $T_B(H,fq)$ an observed brightness temperature at frequency fq and vertical or horizontal polarization. In that study ice types such as white ice (WI: > 0.3 m thickness), grey and grey-white ice (GI: 0.1 - 0.3 m thickness), nilas (NI: < 0.1 m thickness) and open water (OW) were determined visually from Landsat multispectral scanner band 7 (near infrared, 800-1100 nm) imagery for the North Water area, and plotted versus the PR of 18 and 37 GHz (Fig. 3.1). The comparison was made for 260 SMMR grid cells (25x25 km) of the North Water pack ice in spring 1981 for which 100% of the above specified ice types occurred. The decrease of PR with increasing ice thickness could be the result of the reduction in brine volume when the ice becomes thicker and colder, in other words the sensitivity of the vertically polarized brightness temperature to the decrease in salinity. Large variabilities of horizontal polarization is caused by surface roughness on a small scale [Mätzler, 1984]. However, by averaging over a large area (one SMMR pixel), the scatter may be smeared out, and the resulting average value resulting from the thin snow cover and the young ice in the North Water may not be influenced by the disturbing effect.

The standard deviations of open water, nilas and grey ice do not overlap for 18 GHz, indication that a classification of these ice types based on satellite derived PR may be possible over fully consolidated ice (Fig. 3.1). For grey ice and white ice the standard deviations at the same frequency show a small overlap. For 37 GHz however, only water and nilas can be classified accordingly to these PR values with a certain degree of confidence. The standard deviations of the PR values of white ice, grey ice, and to some degree also nilas show a considerable overlap. The larger standard deviation at 37 GHz compared to 18 GHz could be explained by the larger sensitivity of 37 GHz to water vapor; microwave absorption and zenith opacity is three times more sensitive to water vapor at 37 GHz compared to 18 GHz [Walters, 1976]. The standard deviations of open water show a broad range that can be explained by the presence of small ice floes not resolved in the Landsat imagery and by the brightness temperature change due to wind induced spray and foam on the ocean surface.

Similar PR values for the above mentioned ice types were reported by Cavalieri et al. [1986] for aircraft measurements in the Bering Sea, and by Grenfell [1986] for ground based measurements from the Greenland Sea. Radiometric observations of sea ice growth in a tank showed also a decrease of PR with increasing ice thickness, however, the PR reached a limiting value when ice thickness was 20 to 25 mm for air temperatures between -2° to -15° C [Grenfell and Comiso, 1986]. Their study showed also significant changes in PR even though the ice thickness was nearly the same while the air temperature changed by several degrees. For the North Water sea ice, brine volume is assumed to be higher than during the Grenfell and Comiso tank experiment due to the lower air temperatures of -20° to -30° C resulting in a larger difference between horizontally and vertically polarized brightness temperatures.

Based on the relation of increasing polarization ratio with decreasing ice thickness as verified with the Landsat comparison for the North Water area, a threshold technique was applied to classify the different ice types. For the ice typing presented in this paper the following PR values were used for 18 and 37 GHz:

37 GHz	18 GHz
0.086 < OW	0.071 < OW
0.085> NI > 0.031	0.070 > NI > 0.041
0.030 > GI > 0.019	0.040 > GI > 0.023
0.018 > WI	0.022 > WI

The 18 GHz PR is less effected by water vapor (see smaller standard deviation in Fig. 3.1), and therefore, is preferable for applications over polynyas with large amounts of low level clouds due to extensive latent energy flux density. However, the SMMR pixel at 18 GHz has a field of view of 60x60 km, which represents only 50% of the actual power received by the radiometer. The 37 GHz frequency has a field of view of approximately 25x25 km which seems more realistic for young ice classification in polynyas. In the following analysis, the 37 GHz PR were used for ice type classification despite the larger uncertainty due to the considerable overlapping of the PR standard deviation for the different ice types. For winter pack ice conditions with a small fraction of open water and thin ice, this method may give erroneous results because the SMMR pixel of 25 km in dimension is certainly larger than the thin ice areas. To address this problem, the PR of mixed-ice SMMR pixels were analyzed. All SMMR pixels consisting of white ice/grey ice (WIGI), White ice/nilas (WINI), white ice/open water (WIOW) and grey ice/nilas (GINI) of which each ice type, e.g. WI and GI, covered 50% of the SMMR pixel, were classified according to the Landsat data. The PR at 18 and 37 GHz are given in Figure 3.2. Also shown in the figure are the mean PR values for the three ice types and open water. If we compare mean PR only, GI and WIGI signatures are almost identical, and therefore, a clear distinction of ice types and ice type mixtures within one SMMR pixel is not possible. This is the major shortcoming of this proposed PR ice type classification method and limits its application for large homogeneous ice areas consisting of a single ice type which is often found in large polynyas such as the North Water.

3.2.2 Energy Flux Density Parametrization

The method for energy flux density calculation for different first-year ice types is described in detail by Maykut [1986]. Young ice (<0.3 m thick) still has a large conductive energy flux density at the ice/atmosphere interface (Fig. 3.3). Therefore, not only ice-free areas are of importance for energy flux density calculations over pack ice regions. The oceanic energy flux density, the only energy source over Arctic winter pack ice, amounts to 840 W m^{-2} in ice-free regions and as conductive energy flux density to approximately 125 W m^{-2} for young ice areas (Fig. 3.3). Similar results were found during the in situ North Water energy flux density measurements over thin ice [Steffen, 1986]. The conductive energy flux density decreases to about 20 W m^{-2} for ice 2 m thick. The sensible energy flux density in the air which comprises approximately 60 % of the energy loss over young ice, depends mainly on the ambient air temperature, and to a minor degree also on the wind speed. For the calculation of the sensible energy flux density rates of different ice types the monthly mean air temperatures for the North Water region from our three expedition stations

located within that region were used (North Water expedition data archive, ETH, Zürich, Switzerland). The five year data set showed a small interannual variability of the mean monthly air temperature for the months October to March (standard deviation range: ±0.5° and ±1.7° C), and therefore, these mean values were applied for the entire time period shown in this study. The calculated energy flux density rates for the ice types nilas, grey ice, white ice, and open water in dependence of air temperatures for the months November to March are plotted in Figure 3.4. Also shown in Figure 3.4 is the mean monthly air temperature for the North Water region.

3.3 Results

The ice types were classified within the ocean surface of the study area (100,000 km^2) according the method described above. The Smith Sound, Carey Island and Lady Ann Strait polynyas, also located within this study area, vary in size considerably throughout winter. Figures 3.5 give the cumulative ice type percentages for white ice (WI), grey ice/grey-white ice (GI), nilas (NI) and open water (OW) on alternate days for the winter months November to March of 1978/79 to 1985/86. The right abscissa gives the corresponding total energy flux density based on energy flux density parametrization for ice types and open water.

More than 20% young ice (<0.3 m) was found during October to March for most winters, with maximum values of 60% and more. In general the young ice cover in the North Water was decreasing towards the end of the winter. Only a few percent of open water were classified throughout the winter, which is in good agreement with the low level aircraft measurements carried out during the winter 1980/81 (Tab. 5). The large difference between SMMR derived open water and the flight measurement (Dec. 2, 1980, Tab. 5) depicts the limitation of the low resolution passive microwave method, as all open water areas were located along the Greenland coast within the ocean/land SMMR pixel of 25 km.

Date	Julian Day	Open Water (SMMR)	Open Water (Aircraft)
12/2/1980	336	0.0%	5.5%
12/20/1980	354	1.3%	2.9%
12/29/1980	363	0.0%	0.3%
1/22/1981	22	3.3%	4.2%
2/7/1981	38	1.3%	0.0%
3/7/1981	66	0.0%	0.0%

TABLE 5. Open water (OW) derived from 37 GHz passive microwave SMMR data for the North Water area (100,000 km2), compared with open water measured along the flight profile (percent of 1,500 km flight profile) from 300 m altitude with a precision radiation thermometer (PRT-5).

The most striking phenomena is the pulse-like change of ice types throughout winter, which could be explained by strong northerly storms occurring in this region. Wind measurements at Cape Sabine (western side of Smith Sound) carried out during the North Water expedition from

November to March (1974 to 1977) showed a predominantly northerly component with a mean wind speed of 8.7 ms^{-1} from the NNW [Steffen, 1985]. During this period, 14 gales with wind speeds greater then 20 ms^{-1} from the NNW were observed. These storms lasted for a total of 270 hours with maximum wind speeds as high as 40 ms^{-1}. On the average, every tenth day a storm occurred with a mean duration of 19 hours. Because of the ice divergence caused by the wind-induced ice drift of approximately 17 km d^{-1}, the mean duration of stay of sea ice in Smith Sound (northern part of the North Water), between October and March is less than 1 week. These predominantly northerly winds that are channeled in the Smith Sound [Ito, 1982] account for the ice drift which generates open water areas where young ice can grow. The fact that the open water and young ice peaks (maximum extent) occur almost at the same time is due to the size of the study area. A separate study showed (not shown here) that there is a time lag of 2 to 4 days between maximum extents of open water and young ice.

The supply of heat from the sea water and the latent heat of ice formation is compensated by the loss of energy due to sensible heat, latent heat and long wave radiation. This total energy loss due to open water and thin ice is shown in Table 6 (mean for five months period) and in Figure 3.5. The energy loss for the entire North Water region was found to be 77 W m^{-2} for the months November to March. Considering an energy supply by refreezing of 38 W m^{-2}, the remaining 39 W m^{-2} must be withdrawn from the enthalpy in the sea water.

Year	Minimum (Wm^{-2})	Maximum (Wm^{-2})	Mean (Wm^{-2})
1978/79	-60	-176	-88
1979/80	-50	-179	-89
1980/81	-52	-120	-75
1981/82	-50	-233	-87
1982/83	-46	-94	-63
1983/84	-45	-97	-65
1984/85	-46	-101	-65
1985/86*	-55	-152	-81

TABLE 6. Mean energy loss of the North Water surface due to sensible heat, latent heat and long wave radiation. Calculation based on energy flux density rate parametrization for different ice types. (* only November and December)

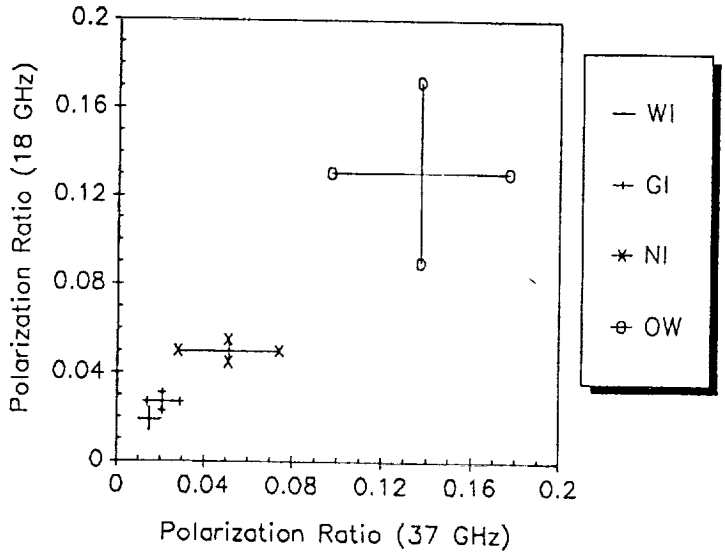

Fig. 3.1 Polarization ratios ± standard deviation at 18 and 37 GHz derived by intercomparison of Landsat and SMMR data for white ice (WI), grey ice/grey-white ice (GI), nilas (NI) and open water (OW).

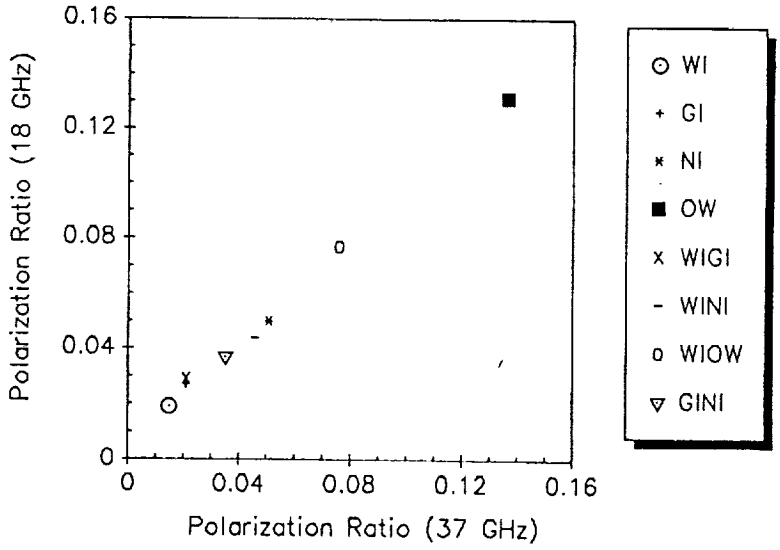

Fig. 3.2 Mean polarization ratios at 18 and 37 GHz derived by intercomparison of Landsat and SMMR data for white ice (WI), grey ice/grey-white ice (GI), nilas (NI), open water (OW), and for mixed-ice SMMR pixels for white ice/grey ice (WIGI), white ice/nilas (WINI), white ice/open water (WIOW) and grey ice/nilas (GINI).

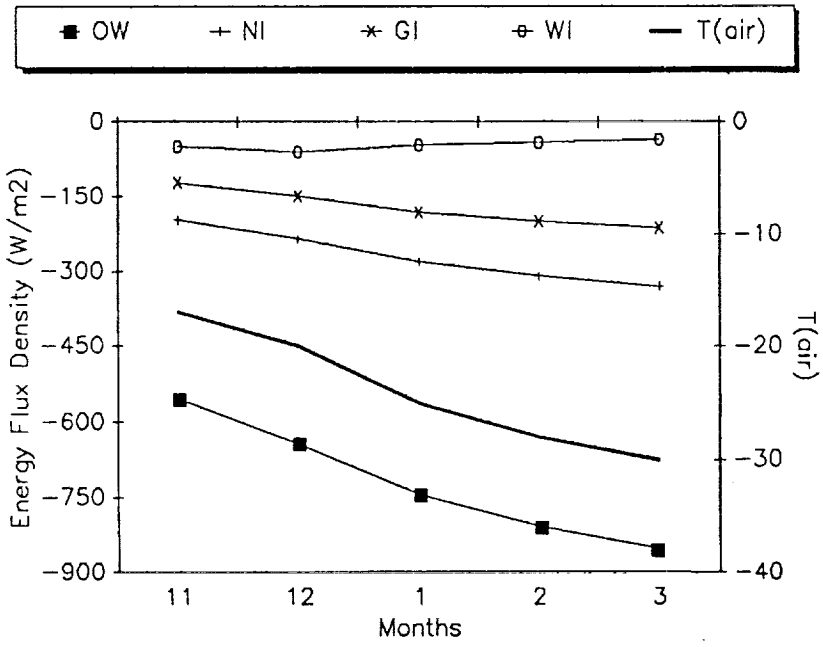

Fig. 3.3 Energy flux density and ice thickness at the ice/atmosphere interface in January for an air temperature of -30 °C [after Maykut, 1986; Steffen, 1986].

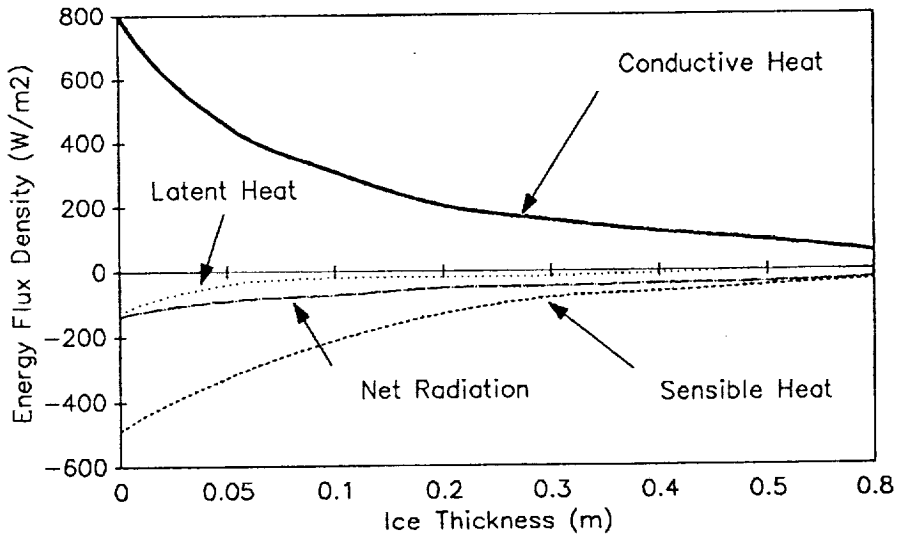

Fig. 3.4 Total energy flux density rates (sensible energy flux density, latent energy flux density and long wave radiation balance) over four different ice types (white ice, grey/grey-white ice, nilas, and open water) during the winter months November to March. The right abscissa shows the local air temperature for the North Water region, as derived from the North Water climate data archive (ETH, Zürich, Switzerland).

Fig. 3.5 Cumulative ice type percentage for white ice (WI), grey/grey-white ice (GI), nilas (NI), and open water (OW) derived from SMMR passive microwave data (19 and 37 GHz polarization ratios) for the North Water area (100,000 km^2), winter 1978/79 to 1985/86. The right abscissa shows the total energy flux density (sensible energy flux density, latent energy flux density and long wave radiation balance) derived from the ice type percentage of the North Water area.

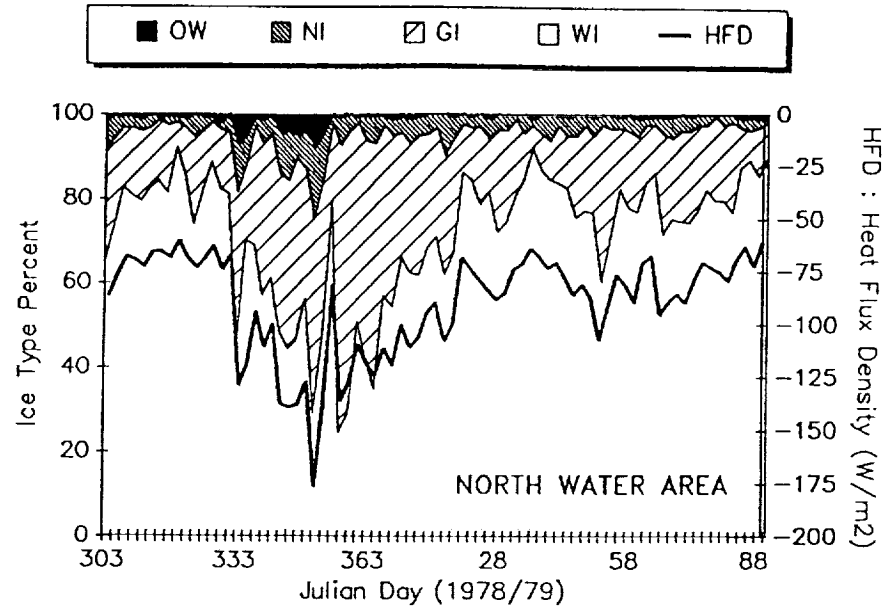

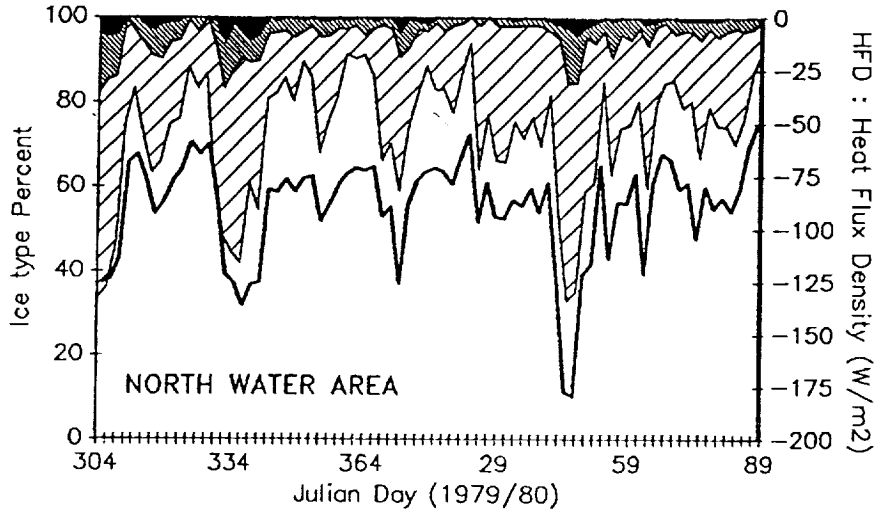

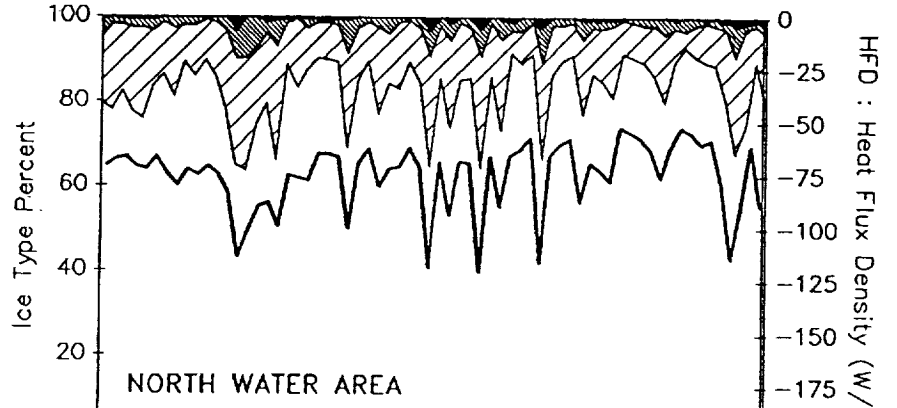

Fig. 3.5 Cumulative ice type percentage for white ice (WI), grey/grey-white ice (GI), nilas (NI), and open water (OW) derived from SMMR passive microwave data (19 and 37 GHz polarization ratios) for the North Water area (100,000 km^2), winter 1978/79 to 1985/86. The right abscissa shows the total energy flux density (sensible energy flux density, latent energy flux density and long wave radiation balance) derived from the ice type percentage of the North Water area.

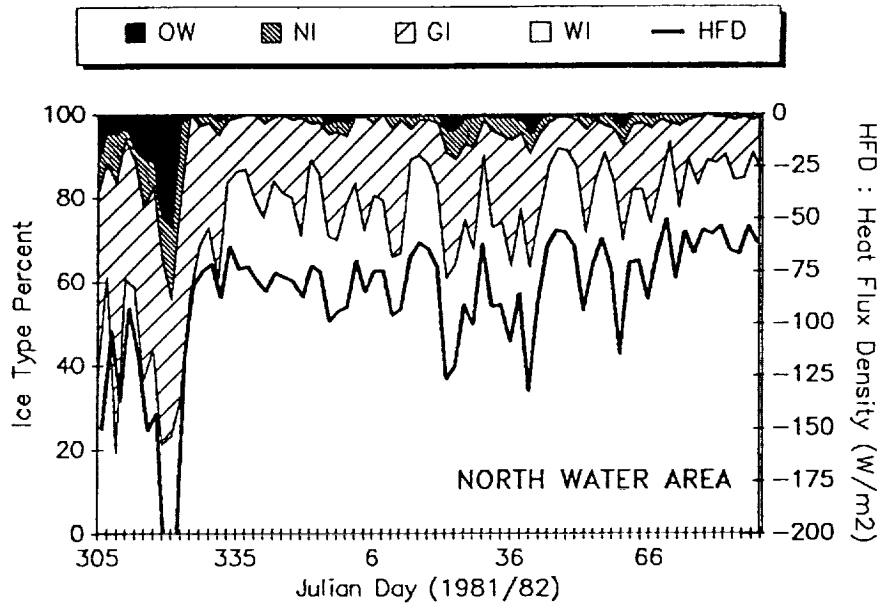

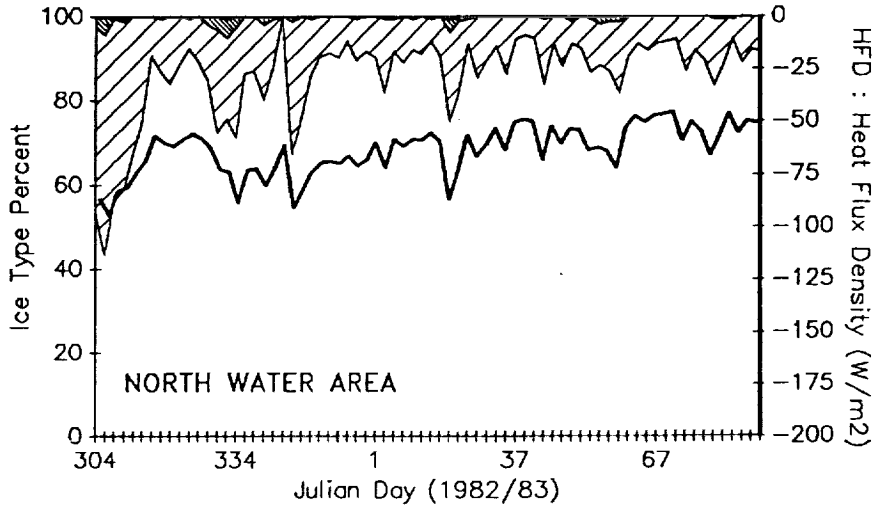

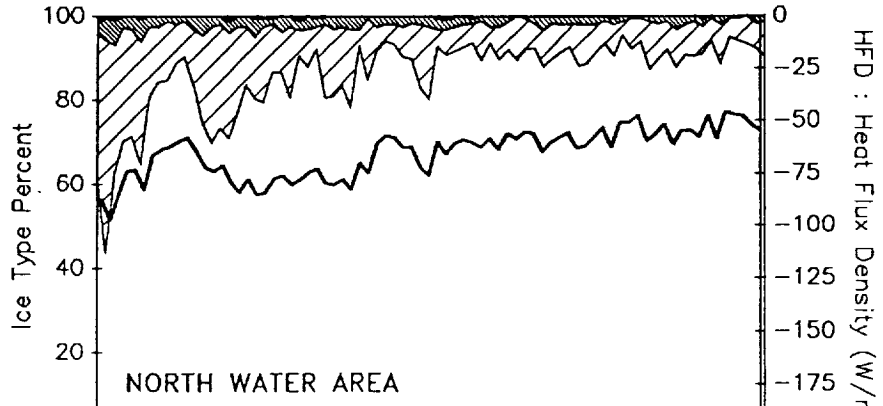

Fig. 3.5 Cumulative ice type percentage for white ice (WI), grey/grey-white ice (GI), nilas (NI), and open water (OW) derived from SMMR passive microwave data (19 and 37 GHz polarization ratios) for the North Water area (100,000 km^2), winter 1978/79 to 1985/86. The right abscissa shows the total energy flux density (sensible energy flux density, latent energy flux density and long wave radiation balance) derived from the ice type percentage of the North Water area.

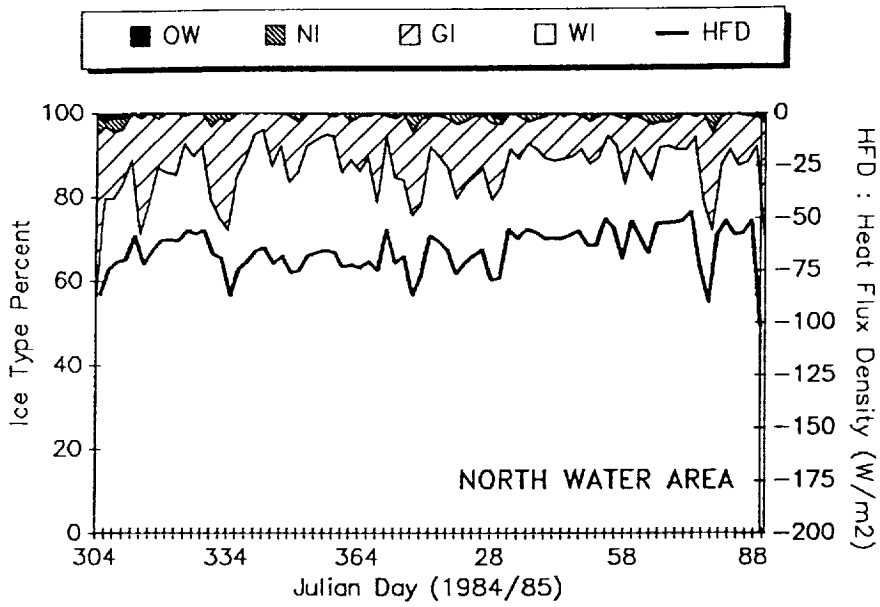

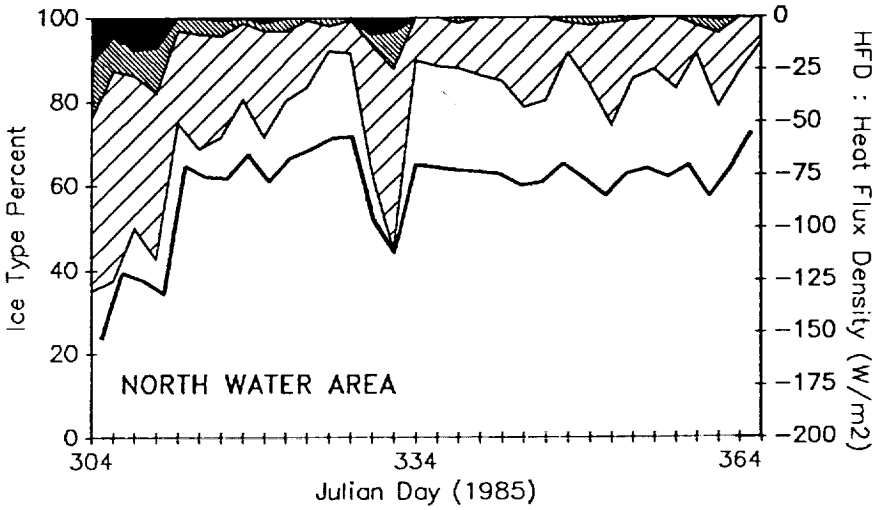

4.0 Fetch and Stability Sensitivity Estimates of Turbulent Heat Flux

4.1 Introduction

In models where open water or thin ice fraction is included in heat flux calculations, bulk aerodynamic formulae, e.g.,

$$H_s = \rho c_p C_{Hr} U_r (T_s - T_r) \tag{4.1}$$

$$H_L = L_v C_{Er} U_r (Qs - Q_r) \tag{4.2}$$

are typically used to represent surface energy transfer. Here, H_s is sensible heat flux, H_L is latent heat flux, ρ is the air density, c_p is the specific heat of air at constant pressure, L_v is the latent heat of vaporization of water, U_r is the wind speed, T_s is the surface water temperature, and T_r is the air temperature. C_{Hr} and C_{Er} are the bulk transfer coefficients for sensible heat and latent heat, respectively. These coefficients are referenced to the height r at which wind speed and temperature are measured or assumed to be representative of local conditions. The transfer coefficients are determined empirically, and include complex interactions between forced convection (mechanical turbulence), free convection (convective turbulence), and scalar roughness lengths. In large-scale sea ice and climate models, values for C_{Hr} and C_{Er} are typically fixed, and do not reflect changes in atmospheric stability or lead width. The objective of this section is to define the sensitivity of flux estimates to these adjustments.

The rate of turbulent heat transfer from leads and polynyas has been shown to be a non-linear function of over-water distance of travel [e.g., Andreas, 1980]. Andreas and Murphy [1986] (referred to here as AM) provide a set of equations to adjust neutral-stability coefficients (C_{HN} and the drag coefficient C_{DN}) to include the effects of atmospheric stability and fetch corrected for reference height. AM discuss how free convection due to the large temperature contrast at the ice/water boundary of a lead or polynya during winter combines with turbulent mixing to increase the values of C_H and C_E over open-water values that arise from forced convection alone. They also note that, as the air mass continues to travel over open water, this instability is eroded, and the free-convection contribution to the heat flux diminishes. As fetch increases and/or -L decreases, C_{HN10} tends toward open-ocean values of about 1.0×10^{-3}. At small nondimensional fetch -X/L, free and forced convection combine to increase energy transfer. Under the same wind and temperature conditions, narrow leads yield a greater flux than do wider leads.

Given that bulk transfer coefficients for turbulent fluxes are treated simplistically in existing models, and that the means described above exist to estimate coefficients that are more appropriate for specific conditions, two questions arise in terms of applications in large-scale sea ice and climate models: 1) under what weather and ice conditions is the need for adjusted coefficients greatest, and 2) in terms of flux estimates over large areas, how important are these adjustments, keeping in mind the penalty of additional calculations? In addition to potentially improving flux treatments in models, answers to these questions will help determine the types of measurements needed from remote sensing, and will help guide the levels of accuracy required from satellite measurements.

4.2 Methodology

To define the critical range for adjusted transfer coefficients, the AM equations are used to calculate coefficients and fluxes under a range of combinations of wind speed, air temperature, fetch, and ice thickness. To assess the significance of these conditions in the Arctic under different lead width regimes, fluxes are calculated using fixed versus fetch and stability adjusted coefficients for a five-year time series of meteorological observations and ice concentration data. The importance of fetch under actual lead width conditions, concentration, and ice thickness is estimated using submarine sonar observations. Since it is useful to consider how this different treatment of turbulent fluxes affects predicted ice thicknesses, the stability and fetch adjustments are coupled to a one-dimensional ice growth model driven by climatological forcing fields. Finally, sonar data and theoretical distributions of lead widths are used to compare the effects of different lead-width parameterization schemes in estimating fetch-sensitive fluxes.

4.2.1 Turbulent Flux Estimates

Bulk transfer coefficients are calculated based on supplied values for U_r, T_s, and T_r. Salinity (S) is used to estimate the freezing temperature of sea water. Lead width and the angle of the wind to the long axis of the lead are also given in order to calculate fetch (X). The methods of calculating the bulk transfer coefficients and heat fluxes follow those in AM. For tests using fixed transfer coefficients, stability and fetch corrections were not applied. Sensible and latent fluxes are then calculated using bulk aerodynamic formulae. Derived conditions are air density, surface vapor pressures over ice and water, vapor pressure at height r over water, and relative humidity (RH).

To study the effects of fetch and stability over refrozen leads, an ice surface temperature is necessary. Surface temperatures for different ice thicknesses were estimated using an energy balance equation coupled to the transfer coefficient calculations described above, with appropriate values for wind speed, surface air temperature, ice and snow conductivities, ice and snow albedos, oceanic flux, longwave flux, and shortwave flux. The energy balance equation used is basically the single-layer model given by Maykut [1982]. A linear temperature profile and no internal heat storage are assumed for the thin ice (0.05 - 1.0 m) we are concerned with here.

Since C_H is a function of surface temperature and vice versa, the energy balance equation was iterated to converge on C_H and T_S. The energy balance equation itself was solved using the Newton- Raphson procedure.

4.2.2 Ice Growth Experiments

To observe how the different flux treatments affects the growth of ice over an annual cycle, we use the three-layer ice growth model of Semtner [1976] coupled to a simple lead model [e.g., Parkinson and Washington, 1979]. The objective is not to predict ice thickness, but rather to observe the magnitude of the change introduced by introducing turbulent flux estimates adjusted for fetch and stability. The formulation used is essentially the one dimensional thermodynamic ice-lead model of

Shine and Crane [1984] and Shine and Henderson-Sellers [1985]. Details of the model can be found in these papers. A specified miminum lead fraction is maintained at all times to simulate dynamic processes. The complex treatment of surface albedos described in Shine and Henderson-Sellers [1985; Table 4] is used. Incoming shortwave radiation was calculated at 80° N, with the adjustments used by Shine and Crane [1984] to take into account flux changes between clear and cloudy skies. A mean optical thickness for Arctic clouds is taken to be 7.5. Longwave fluxes from climatology were used in place of the longwave calculations described in Shine and Crane [1984]. The prescribed forcing fields for shortwave radiation, longwave radiation, air temperature, and relative humidity are given in Table 1. These values were estimated from the data in Table 1a of Maykut [1982], which were derived from the results of Doronin [1963] and Marshunova [1961]. In the Shine model, these mid-monthly values are interpolated to eight hour time-steps using a cubic polynomial interpolation.

4.2.3 Lead Width Parameterization

Finally, given the relationships between atmospheric stability, lead width, and heat flux estimates, a question arises regarding the use of a single value for lead width to represent some sense of an average over a region, or a distribution of lead widths. To address the question of how lead width distributions might best be included in the turbulent flux estimates, a method is needed to compare fluxes using a single fetch versus fluxes integrated over a distribution of fetches.

4.3 Data

In addition to the climatological forcing fields used in the Shine model, meteorological data, lead width, and ice thickness data are needed to extend the sensitivity calculations beyond theoretical conditions. The meteorological data sets used include gridded pressure and temperature fields provided by the Arctic Ocean Buoy Program [commencing with Thorndike and Colony, 1980]. These data are derived from pressures and temperatures recorded by drifting buoys, which are then combined with NMC station data gridded using an optimal interpolation method that takes into account the spatial autocorrelation of the meteorological fields. The gridded temperatures therefore include whatever error is contained in the NMC station data. Daily pressure and temperatures for 12 GMT were extracted from these data tapes for the period from 1 January 1979 - 30 November 1984. Geostrophic winds were calculated from the buoy-measured sea level pressures. Buoy-measured temperatures are internal "box" temperatures and are subject to errors of several degrees, mainly due to radiational heating within the buoy housings, and thus are not direct measurements of snow cover temperatures or air temperatures [Thorndike and Colony, 1980]. Errors are expected to be biased toward overestimates of air temperatures during summer, and also during winter if the buoys are insulated by drifted snow. During spring of 1979, Thorndike [1980] notes diurnal temperature fluctuations of about 4° C, while during dark periods the buoy temperatures and air temperatures a half-meter above the ice-snow surface probably agree to within about 1° C.

The meteorological information was mapped from latitude and longitude coordinates to a polar stereographic grid with a 200 km x 200 km cell size true at 70° N. A simple nearest-neighbor resampling was used to assign data values to grid positions. For this investigation, we focus on data for a single grid cell centered at approximately 80° N, 155° W. The buoy-derived geostrophic wind speeds require scaling by an appropriate reduction factor to yield wind speeds closer to those expected at a 10 m height. Wind speed measurements during AIDJEX [Albright, 1980] show a ratio of observed surface winds to calculated geostrophic winds of 0.585 for an annual average. We use this value to reduce our geostrophic wind speeds to values more appropriate for the heat flux calculations.

Distributions of lead widths and spacings have not been studied extensively, and statistics are available for only a few geographic areas and times. The statistics used in this study are based on submarine sonar data, in particular that recorded by the USS QUEENFISH across the Canada Basin in early August, 1970 [McLaren, 1989], with a narrow- beam, upward-looking acoustic profiler. Data were interpolated to 1.45 m intervals. The accuracy of the acoustic profiler is ± 0.15 m at best; the precision of the interpolation routine is estimated to be ± 10 mm.

Since the profiler has an inherent vertical error, it is not possible to know in most cases if a data point recorded as 0 draft is in fact open water. We therefore define leads in terms of maximum drafts of 0.30, 0.70, and 1.00 m in the table. The distribution of draft values within each of these bins is quite variable with the mean draft being 40-60% lower than the maximum in each case. The implication of using these definitions of leads for heat flux calculations is obvious, but our purpose is only to obtain typical width estimates and a width distribution model for heat flux sensitivity tests. An additional uncertainty is introduced due to the unknown lead crossing angle. Unfortunately, no coincident overhead satellite or aircraft data is available, so the true lead widths are unknown. However, width distribution shapes are similar across the track and compare favorably to those measured in other studies, so that their use is not unreasonable.

4.4 Results

Four major questions are addressed here: 1) under what conditions are sensitivities to fetch and stability corrections greatest, 2) how significant are these conditions in reality, 3) how substantial a change in mean ice growth is introduced by adjusting the turbulent flux estimates, and 4) how simple can a treatment of fetch be to reasonably represent variations in fetch for estimates of mean fluxes over large areas? The first item is addressed using the AM procedure coupled with the energy balance equation to calculate bulk transfer coefficients and turbulent fluxes for a range of fetches, ice thicknesses, wind speeds, and air temperatures. Then, the same procedure is combined with the time-series of drifting buoy data and the sonar-derived lead statistics to determine how fluxes and ice growth rates are affected in observed conditions. Thirdly, the thermodynamic ice growth model is used to study the effects of varying fluxes on monthly mean ice thicknesses. Finally, comparisons are made between fluxes calculated using observed lead width distributions, theoretical distributions, and distribution means.

4.4.1 Sensitivity to Fetch, Wind Speed and Temperature

C_H generally increases with decreasing air temperature, decreasing fetch, and decreasing wind speed. The sensitivity of C_H to fetch increases with decreasing wind speed and with increasing T_s-T_a. One way of considering the AM adjustments to the bulk transfer coefficients is to treat the adjustments as a mixture of the rate of free convection versus forced convection, scaled by fetch. For example, under light winds, the large temperature contrast over leads in winter allows free convection to persist over a longer fetch. In strong winds, turbulent mixing breaks down the surface-to-air temperature contrast, and forced convection becomes dominant. For narrow leads, turbulent flux is enhanced due to the combination of free and forced convection while, for larger leads, free convection is reduced.

For weakly unstable conditions (T_a = -5 C), fetch dependency is small for relatively high wind speeds (> 10 m s^{-1}). At U = 10 m s^{-1}, C_{H10} decreases by 4% as fetch increases from 10 m (C_{H10} = 1.96x10^3) to 200 m (C_{H10} = 1.88 x 10^3). However, at U = 3 m s^{-1}, C_{H10} decreases by 32% as fetch increases from 10 m (C_{H10} = 2.52x10^3) to 200 m (C_{H10} = 1.71x10^3). As instability increases, fetch dependency also increases, with the greatest fetch dependency at lower wind speeds. The rapid drop-off in C_{H10} with increasing fetch at lower wind speeds can be explained as the effect of a decrease in forced convection combined with reduced free convection as the temperature contrast erodes as the over water distance increases.
For T_a = -30 °C and U = 5 m s^{-1}, conditions typical of the central Arctic during winter, C_{H10} ranges from 2.96x10^3 at X = 10 m, to 1.54x10^3 at X = 200 m. One can compare this to the C_{H10} value of 3.0x10^3 used by Maykut [1982] for open water leads and thin ice. For the same T_a, an increase in wind speed to 10 m s^{-1} reduces C_{H10} to 2.47x10^3 at 10 m to 1.76x10^3 at 200 m.

Since C_{H10} increases as both U and T_a decrease, the effects on calculated turbulent fluxes are not direct. The change in C_{H10} translates directly to the same proportional change in turbulent flux. However, although the greatest change in C_{H10} occurs as T_a decreases, this change is also maximum at lower wind speeds. Since flux decreases with wind speed, the overall effect on H_s and H_l of the C_{H10} change is also reduced. In contrast, the small changes in C_H at high wind speeds, combined with the enhanced flux at high wind speeds, yield substantial changes in total turbulent flux. At T_a = -30° C, the greatest change in H_s between H_s at 10 m and 200 m occurs at U = 5 m s^{-1} (a decrease of 48%). This decrease drops with wind speed, to 9% at U = 20 m s^{-1}. Under weakly unstable conditions, the change in C_H from 10 m to 200 m fetch reduces H_S by 15% at U = 5 m s^{-1}, and 1% at U = 20 m s^{-1}. Since H_S is lower under these conditions, the absolute change in H_S is also less.

The interactions between wind speed, stability, and the drag coefficients are complex can be better understood by considering the relationship between Ri_B and the stability parameter . For the sample data used by AM. Based on the suggested relationships of Panofsky [1969] between atmospheric mixing and Ri_B, -0.03 < Ri_B < 0 indicates a combination of forced and free convection, with forced convection dominating. For Ri_B < -0.03, free convection dominates the turbulent mixing process. Thus, as Ri_B increases, L decreases, the nondimensional fetch X/L becomes increasingly

negative, and C_{HN10} decreases. $-Ri_B$ increases as U and T decrease or as $T_s - T_r$ increases. For short fetches, forced convection acts to increase the efficiency of free convection, yielding an overall increase in C_{HN10}. L does not vary with fetch, e.g., the modification of T_a downwind is not treated; however, since the estimated C_{HN10} represents an average for the entire lead, inclusion of the fetch X effectively parameterizes the reduction in C_{HN10} observed with decreasing fetch.

Andreas [1980] discuss relationships between a fetch-dependent Reynolds number and a Nusselt number for sensible heat flux. He developed both an exponential relationship,

$$N = 0.08 R_x^{0.76} \tag{4.3}$$

and a linear form,

$$N = 1.8 \times 10^{-3} R_x + 1100 \tag{4.4}$$

McBean [1986] and Smith et al. [1990] used the linear form to show that the average heat flux from a lead is independent of fetch when fetch exceeds about 30 m. However, Andreas [1980] notes that the data used to develop these relationships do not support choosing between the linear and exponential forms (the observations did not include fetches greater than 35 m), although he states that the exponential equation appears more physically reasonable over a large Reynolds number range. Applying the same approach to the exponential form as was applied to the linear form by McBean [1986] yields

$$H_S = [0.08 (U X/)^{0.76}]/X [(T_o - T_2)]/X \tag{4.5}$$

where is the thermal conductivity of air and is the kinematic viscosity of air. For a wind speed of 3 m s^{-1} and a difference in air temperature of 19° C, the average flux from a lead estimated using the linear equation [McBean, 1986] decreases by only 4% as fetch increases from 33 m to 100 m. However, if the exponential form is used, the decrease is 17%. For a fetch of 1000 m, the predicted fluxes yield CH values of 2.5×10^{-3} for the linear relationship, and 1.1×10^{-3} for the exponential form. While 1000 m is well outside the range of observations used to develop these Nusselt number relationships, the fact that the exponential form yields a transfer coefficient that approaches the expected open-ocean coefficient of about 1.0×10^{-3} suggests that exponential form may be more realistic. Sensible fluxes predicted using the fetch and stability-adjusted coefficients from the AM approach were compared to fluxes estimated using the Nusselt number relationships given above for a wind speed at 2 m = 5 m s^{-1}, Tr = -33.4 °C, Ts = -1.8 °C, P = 1013 mb, and RH = 90%. Both the exponential equation from Andreas [1980] and the fetch and stability-adjusted form (AM) show a sensitivity to fetch well beyond 35 m. Strong free convection under the given conditions act to keep the fetch and stability-adjusted fluxes high. The effect of thin ice in a lead is to decrease the surface temperature-air temperature differential by decreasing the surface temperature. The effect on the fetch and stability-adjusted coefficients is nearly equivalent to the effect on the coefficients of an increase in air temperature over open water.

Actual ice conditions consist of a mixture of open-water leads and refrozen leads covering a range of widths and ice thicknesses. To test the sensitivity of turbulent fluxes to adjusted transfer coefficients over such an ensemble of leads, sonar data covering 150 km from the USS QUEENFISH track were processed to generate lead widths grouped by mean lead width and ice thickness categories. T_a, F_r, and F_L from Table 1 for October were supplied to the energy balance procedure outlined in earlier to calculate ice surface temperatures and turbulent fluxes based on a fixed transfer coefficient (3×10^{-3}) and fetch and stability-adjusted coefficients. In the 150 km transect, 2.6% of the transect length is made up of leads with ice thicknesses less than or equal to 0.8 m. The sonar data indicate that less than 1% of this lead area is open water (0 - 0.05 m ice). 81% of the leads (39% of the lead-covered area) are less than 20 m wide. The widest lead is between 340 m and 360 m. Sensible fluxes from the lead-covered area averaged 79.6 W m^{-2} using a fixed transfer coefficient compared to 64.6 W m^{-2} with adjusted coefficients; use of the adjusted coefficients; a 19% decrease in flux per lead-covered area. An areally-weighted average over the 150 km transect (taken to be 1 m wide) yields a total of 1.9 W m^{-2} using a coefficient of 3×10^{-3}, and 1.605 W m^{-2} with adjusted coefficients.

4.4.2 Sensitivity Under Observed Conditions

Using the daily buoy temperatures, wind speeds, and air pressures for 1979-1984, a series of daily-adjusted bulk transfer coefficients and turbulent fluxes were calculated for a range of fetchs for fluxes per unit area over open water. For fluxes over different ice thicknesses, these data are combined with the longwave and shortwave forcings given in Table 1. Monthly averaged fluxes calculated using a fixed transfer coefficient of 3×10^{-3} are about 8% greater than fluxes calculated with a fetch of 10 m, about 27% greater than fluxes estimated with a 50 m fetch, and about 35% greater than fluxes for a 100 m fetch. For refrozen leads, the percent change with fetch decreases. The magnitude of the change also decreases with the decrease in surface temperature for thicker ice within the lead. For example, the change in sensible heat flux using a 10 m fetch vs. a 50 m fetch is about 9% for an ice thickness of 0.15 m. In January, this difference is about 10 W m^{-2}. Thus, the decrease in fetch sensitivity with an increase in ice thickness shown earlier translates into a similar decrease in sensitivity using observed forcings.

ICE THICKNESS ESTIMATES

The thermodynamic ice growth model was driven using fluxes calculated with the AM procedure for an open-water fetch of 10 m and 100 m, with a mean wind speed of 5 m s^{-1} and the monthly air temperatures in Table 1. The resulting total turbulent fluxes (sensible + latent) as well as the net surface shortwave flux and downwelling longwave flux estimated in the model are given in Table 1. Turbulent fluxes from 100 m leads average 37% less annually than fluxes from 10 m leads. Mean annual ice thickness decrease by 21% from 3.92 m to 3.10 m. The greatest difference occurs during autumn, when mean monthly ice thicknesses predicted using a 100 m fetch are 23% less than that for 10 m fetch. As a comparison, a decrease in monthly air temperatures by 2 degrees increases mean annual ice thickness by 3.6% for a 100 m fetch. At these temperatures, the decrease in fetch from 100 m to 10 m produces a 29.9% increase in ice thickness. An increase in wind speed from 5 m s^{-1} to 6 m s^{-1} increases the mean annual ice thickness by 9.9%. This model

demonstrates in a simplistic way the direct effect of increased cooling of the ocean surface due to enhanced turbulent fluxes from narrower leads. Since no atmospheric coupling exists in the model, any increase in T_a due to this enhanced energy loss from the ocean is ignored.

TREATMENT OF LEAD WIDTHS IN FLUX ESTIMATES

The question here is the difference introduced by calculating fluxes using an approximation of lead width conditions, compared to fluxes calculated using actual conditions. This approximation could take the form of a theoretical distribution that approximates the actual lead conditions, or some other measure, such as the mean lead width.

As a first step, observed lead width distributions were compared to the theoretical negative exponential and lognormal models. In general, there are more small lead widths than expected with the negative exponential model, although approximately 25% of the observed distributions appear to fit this model at the 0.1 level of significance. Distributions for different maximum draft/minimum width pairs vary significantly only when the number of leads in a category is too small to provide a reliable sample. Other studies provide similar descriptions of lead widths and distributions.

Comparisons of the fluxes calculated using actual distributions, theoretical distributions, and a basic descriptor (in this case, the distribution mean) were performed by combining a lead distribution summation with the AM model described earlier. In the simplest case, the total flux was calculated using a mean lead width. In the second case, a flux was calculated at each lead width and summed to yield an average flux for the given set of leads. Finally, fluxes were calculated and integrated over the theoretical distributions using Simpson's Rule. Each set of calculations was done under a range of wind speed and air temperatures to determine the sensitivity of the different lead treatments to meteorologil conditions. The results are summarized in Table 3. In short, fluxes calculated from the theoretical distribution constructed from the mean as well as fluxes estimated using only the mean agree well with the fluxes summed over the actual distribution.

4.5 Summary

Preliminary conclusions suggest a significant value in adjusting bulk transfer coefficients for stability. Correction for fetch can also be significant under conditions typical of Arctic mid-winter conditions (e.g., relatively light winds and low air temperatures). Fetch corrections become less important as ice thickness increases in refrozen leads. In terms of remote sensing requirements, factors such as ice thickness and open water distributions can outweigh changes due to fetch effects. However, if surface conditions are known, it may be more important to accurately treat fetch sensitivity than to attempt to improve temperature or wind speed observations by a few degrees or 1-2 m s^{-1}. A more complete analysis of these results is underway.

Months -->	Jan.	Feb.	March	April	May	June	July	Aug.	Sept.	Oct.	Nov.	Dec.
Cloud Amount	0.50	0.47	0.54	0.47	0.72	0.82	0.87	0.89	0.85	0.78	0.47	0.45
T_a(°C)	-29.4	-32.0	-31.2	-22.7	-10.5	-1.2	-0.6	-1.4	-9.9	-19.8	-27.8	-29.2
RH	0.85	0.85	0.88	0.88	0.89	0.93	0.93	0.94	0.88	0.85	0.85	0.85
H(w) (W m^{-2}), 10 m	-665.1	-725.2	-706.8	-507.1	-210.7	1.1	9.8	-2.3	-196.1	-437.5	-627.7	-660.4
H(w) (W m^{-2}), 100 m	-398.9	-425.8	-417.5	-327.4	-169.6	1.1	13.5	-2.2	-160.1	-294.5	-382.1	-396.8
H(i) (W m^{-2})	16.5	14	10.5	2	-12	-18	-18	-16	-9	1	8.5	14
F_L (MJ m^{-2} mo^{-1})	446	423	448	487	635	753	808	789	687	587	464	453
F_r (MJ m^{-2} mo^{-1})	0	0	12	58	105	191	281	178	27	1	0	0

Table 1. Monthly averages and totals for quantities used as input to the one-dimensional ice growth model.
F_L downwelling radiation
F_r net surface radiation

Months -->	Jan.	Feb.	March	April	May	June	July	Aug.	Sept.	Oct.	Nov.	Dec.
F_L (MJ m^{-2} mo^{-1})	168	166	166	191	244	289	309	301	267	223	184	174
F_r (MJ m^{-2} mo^{-1})	0	0	39	162	281	302	223	142	60	8	0	0

Table2. Monthly averages of F_L and F_r used for surface energy budget calculations with the time-series of buoy data.

Max Draft		A	B	C	D	E	F	G	H
0.3	Lead Width (m)	26.5	33.1	21.3	26.5	4.7		18.5	23.8
0.3	Stand. Dev.	2.1	2.9	2.4	2.6	7.1		2.6	3.7
0.3	Maximum (m)	228	502	130	283	327		70	90
0.7	Lead Width (m)	32.6	54.8	27.5	32.1	49.4	36.4	34.7	40.0
0.7	Stand. Dev.	3.3	3.8	2.0	2.8	7.0	8.3	3.8	3.7
0.7	Mamimum (m)	885	526	255	294	374	537	257	227
1.0	Lead Width (m)	28.9	40.8	32.9	30.9	50.5	32.4	36.4	40.0
1.0	Stand. Dev.	2.4	2.5	2.5	2.2	6.5	6.6	3.7	3.6
1.0	Maximum (m)	886	533	7634	299	374	539	263	269

Table 3. Lad widths (m) and standard deviations in the QUEENFISH data by region and maximum draft (m). Also given are the maximum lead widths encountered. Minimum width used in the definition is 3 m, corresponding to the footprint of the sonar instrument. No statistics are given if fewer than 20 leads were found in a region. Regions are each approximately 150 km in length and extend from the southern Canada Basin (A), the North Pole (G) and beyond (H) along the 155th meridian.

5. Surface Temperature Algorithm

5.1 Objective

The retrieval of ice-surface tempartures from satellite imagery provides important information for calculating the surface energy balance in the Arctic regions. Given a measured ice surface temparture, radiative and turbulent fluxes may be calculated. The following paragraphs will outline the approach and initial experiments towards developing an ice temperature algorithm based on advanced very high resolution radiometer (AVHRR) data.

5.2 Methodology and Data

Measured AVHRR radiances in thermal bands 3 (3.55 - 3.93 μm), 4 (10.5 -11.3 μm) and 5 (11.5 - 12.5 μm) are related to surface temperatures through the the surface emissivity ε, the Plank function B(T), as well as the radiative properties of the overlying atmosphere through (5.1)

$$I = \varepsilon B(T) + (1-\varepsilon)\,\tau_0^H \int_H^0 B(T(\eta))\,\frac{\delta\tau(\eta)}{\delta\eta}\delta\eta + \int_0^H B(T(\eta))\frac{\delta\tau(\eta)}{\delta\eta}\delta\eta \qquad (5.1)$$

where B(T) is the Plank function, τ_H^0 transmissivity of the atmosphere and ε the emssivity of the surface.

For the retrieval of surface temperatures this equation needs to be inverted from the received radiances in several spectral bands of the AVHHR sensor. To achieve an accurate retrieval of surface temperatures, a correction for the radiative effects of the atmosphere has to be incorporated. This atmospheric correction can be computed through the combination of several spectral bands. In analogy to the retrieval of sea surface temperatures over the open ocean, this will be achieved through the computation of empirical functions based on detailed radiative transfer calculations using Lowtran 7 atmospheric correction model. Model radiances for the spectral bands corresponding to channels 3, 4 and 5 of the AVHRR sensor are computed for a range of surface temperatures and environmental conditions. An empircial function is then fit to the computed radiances and surface temperatures, so that

$$DT = \text{Min} = \sum_{i=0}^{N} (T_{model}(I_3,I_4,I_5) - T_{emp}(I_3,I_4,I_5))^2 \qquad (5.2)$$

where T_{emp} empircal function of format $F(x,y,z) = a_1 + a_2x + a_3y + a_4z + ...$

T_{model} temperatures used for modelling Lowtran-7 radiances

I_3,I_4,I_5 modelled radiances

T_{emp} in combination with measured AVHRR radiances can then be used to calculate surface temperatures. In order to define empircal functions that are suitable for a polar atmosphere, radiative transfer calculations need to be conducted using profiles that are representative for the environmental conditions prevailing in the regions under investigation. Since Lowtran 7 's standard configuration only contains a profile for a standard subarctic atmosphere, atmospheric profiles measured by radiosonde from a data set currently being compiled by Serreze et. al (pers. Comm) were utilized for some initial calculations. A total of 134 observations from an ice island located at 82° N and 176° W during the winter month of 1986 and 1987 were used to calculate integrated radiances for AVHRR channels 3, 4, 5 and longwave broadband from 0.4 to 50 µm. Each calculation was done for 5 sensor viewing angles : 0°, 10° ,20° ,30° and 40°.

5.3 Results

Using a simple multiple-linear regression as the empirical function for surface temperature retrieval an excellent correspondence between surface temperature (temperature at lowest level of radiosonde profile) and modelled radiances can be achieved (R-square 0.9998). This strong correlation, while in principle not surprising, indicates the general possibility of inverting the equation of radiative transfer through a linear parameterization for Arctic atmospheres.

Future Plans

- In order to validate the above outlined technique using an independent data set, similar calculations are planned using profiles obtained by the 1990 Greenland Expedition of the Climate Research Group at the Swiss Federal Institute of Technology. This data set contains radiosonde profiles in addition to simultaneous measurements of radiative and turbulent fluxes. Since this data set includes in situ measurements of skin-temperature, it should provide an opportunity to validate the ice surface temperature algorithm under development.

- Modelling experiments will be conducted to investigate the feasability of computing incoming and outgoing longwave radiation based on AVHRR data under clear and cloudy conditions.

6. References

Andreas, E.L. Estimation of heat and mass fluxes over Arctic leads. *Mon. Wea. Rev.*, 108, 2057-2063, 1980.

Andreas and Murphy. Bulk transfer coefficients for heat and momentum over leads and polynyas, *J. Phys. Oceanography*, 16(11), 1875 -1883, 1987.

Cavalieri, D.J., P. Gloersen, and W.J. Campell. Determination of sea ice parameters with Nimbus 7 SMMR. *J. Geophys. Res.* 89, 5355-5369. 1984.

Cavalieri, D.J., P. Gloerson, and T.T. Wilheit. Aircraft and satellite passive microwave observations of the Bering sea ice cover during MIZEX West. *IEEE Trans. Geosci. Remote Sensing*, GE-24(3), 368-377, 1986.

Comiso, J.C. Characteristics of arctic winter sea ice from satellite multispectral microwave observations. *J. Geophys. Res.*, 91(C1), 975-994, 1986.

Crocker, G.B. A physical model for prediction the thermal conductivity of brine-wetted snow. *Cold Regions Sciene Technology*, 10(1), 69-74, 1984.

Doronin,Ya.P. On the heat balance of the Central Arctic (in Russian), *Proc. Arctic Antarctic Res. Inst.*, 253,178-184, 1963.

Gloersen P., and D.J. Cavalieri. Reduction of weather effects in the calculation of sea ice concentration from microwave radiances. *J. Geophys. Res., 91(C3)*, 3913-3919, 1986.

Grenfell, T.C. Surface-based passive microwave observations of sea ice in the Bering and Greenland Sea. *IEEE Trans. Geosci. Remote Sensing*, GE-24(3), 378-382, 1986.

Grenfell, T.C., and J.O. Comiso. Multifrequency passive microwave observations of first-year ice grown in a tank. *IEEE, Trans. Geoscience and Remote Sensing*, GE-24(6), 826-831, 1986.

Hall, R.T. AIDJEX modelling group study involving remote sensing data; in : Pritchard R.S. (ed) *Sea ice Processes and Models*. University of Washington, Press, Seattle, 151-162, 1980.

Ito, H. Wind through a channel surface: Wind measurements in Smith Sound and Jones Sound in the northern Baffin Bay. *J. Appl. Meteorol.*, 21, 1053-1062, 1982.

Mätzler, CH., R.O. Ramseier, and E. Svendsen. Polarization effects in sea-ice signatures. *J. Oceanic Engineering*, OE-9(5), 333-338, 1984.

Maykut, G.A. Energy exchange over young sea ice in the Central Arctic. *J. Geophys. Res., 83*, 3646-3658, 1978.

Maykut, G.A. Large-scale heat exchange and ice production in the Central Arctic. *J. Geophys. Res.*, 87 (C10), 7971-7984, 1982.

Maykut, G.A. The surface heat and mass balance, The Geophysics of Sea Ice (ed. N. Untersteiner). *NATO ASI Series, Series B: Physics*, 146, 395-464, 1986.

McBean, G. The atmospheric boundary layer, in *The Geophysics of Sea Ice*, edited by N. Untersteiner, pp. 283-337, Plenum, New York, 1986.

McLaren, A.S. Analysis of the under-ice topography in the Arctic Basin as recorded by the USS NAUTILUS, August 1958, *Arctic*, 41, 117-126, 1988.

McLaren, A.S. The under-ice thickness distribution of the Arctic Basin as recorded by USS NAUTILUS in 1958 and USS QUEENFISH in 1970, *J. Geophys. Res.*, 94 (C4), 4971-4983, 1989.

Panofsky, H.A. Air pollution meteorology, *Am. Scientist,* 52 (2), 269-285, 1969.

Parkinson, C.L., J.C. Comiso, H.J. Zwally, D. J. Cavalieri, P Gloersen, and W.J. Campell. Arctic Sea Ice, 1973-1976: Satellite passive-microwave observations, *NASA SP-489*, 1987.

Smith, S.D., R.D. Muench, C.H. Pease. Polynyas and leads: An overview of physical processes and environment. *J. Geophys. Res.*, 95 (C6), 9461-9479, 1990.

Steffen, K. Warm water cells in the North Water, northern Baffin Bay during winter. *J. Geophys. Res.*, 90(C5), 9129-9136, 1985.

Steffen, K. Ice conditions of an Arctic polynya: North Water in Winter. *J. Glaciol.*, 32(112), 383-390, 1986.

Steffen, K., and J.A. Maslanik. Comparison of geophysical sea ice parameters derived from passive microwave data and Landsat imagery for the North Water area of Baffin Bay. *J. Geophys. Res.,* 93(C9), 10769-10781, 1988.

Steffen, K., and A. Schweiger. A multisensor approach to sea ice classiication for the validation of DMSP-SSM/I passive microwave derived sea ice products. *Photogr. Engi. Rem. Sens.,* 56(1), 75-82, 1990.

Steffen K., and A. Schweiger. submitted. DMSP-SSM/I NASA algorithm validation using Landsat satellite imagery. *J. Geophys. Res.*

Weller, G. Radiation flux investigation, *AIDJEX Bull.*, 14, 28-30, 1972.